

1

Physics-dynamics coupling with element-based high-order Galerkin 2 methods: quasi equal-area physics grid

3 Adam R. Herrington*

4 *School of Marine and Atmospheric Sciences, Stony Brook University, Stony Brook, New York,
5 USA.*

6 Peter H. Lauritzen

7 *Climate and Global Dynamics, National Center for Atmospheric Research, 1850 Table Mesa
8 Drive, Boulder, Colorado, USA.*

9 Mark A. Taylor

10 *Sandia National Laboratories, Albuquerque, New Mexico, USA.*

11 Steve Goldhaber, Brian E. Eaton and Julio T. Bacmeister

12 *Climate and Global Dynamics, National Center for Atmospheric Research, 1850 Table Mesa
13 Drive, Boulder, Colorado, USA.*

14 Kevin A. Reed

15 *School of Marine and Atmospheric Sciences, Stony Brook University, State University of New
16 York, Stony Brook, New York.*

17 Paul A. Ullrich

¹⁸ Department of Land, Air and Water Resources, University of California, Davis, California, USA.

¹⁹ *Corresponding author address: Adam R. Herrington, School of Marine and Atmospheric Sciences, Stony Brook University, Stony Brook, New York, USA.

²⁰ E-mail: adam.herrington@stonybrook.edu

ABSTRACT

Atmospheric modeling with element-based high-order Galerkin methods presents a unique challenge to the conventional physics-dynamics coupling paradigm, due to the highly irregular distribution of nodes within an element and the distinct numerical characteristics of the Galerkin method. The conventional coupling procedure is to evaluate the physical parameterizations (*physics*) on the dynamical core grid. Evaluating the physics at the nodal points exacerbates numerical noise from the Galerkin method, enabling and amplifying local extrema at element boundaries. Grid imprinting may be substantially reduced through the introduction of an entirely separate, approximately isotropic finite-volume grid for evaluating the physics forcing. Integration of the spectral basis over the control-volumes provides an area average state to the physics, which is more representative of the state in the vicinity of the nodal points rather than the nodal point itself, and is more consistent with the notion of a ‘large-scale state’ required by conventional physics packages.

This study documents the implementation of a quasi-equal area physics grid into NCAR’s Community Atmosphere Model with Spectral Elements, and is shown to be effective at mitigating grid imprinting in the solution. The physics grid is also appropriate for coupling to other components within the Community Earth System Model, since the coupler requires component fluxes to be defined on a finite-volume grid, and one can be certain that the fluxes on the physics grid are indeed, volume-averaged.

43 **1. Introduction**

44 An increasing number of numerical methods publications in the atmospheric science literature
45 concern transport, shallow-water, and three-dimensional models employing element-based high-
46 order Galerkin discretizations such as finite-element and discontinuous Galerkin methods (for an
47 introduction to these methods see, e.g., Durran 2010; Nair et al. 2011; Ullrich 2014). Some global
48 models based on Galerkin methods have reached a level of maturity for which they are being con-
49 sidered for next generation climate and weather models due to their inherent conservation proper-
50 ties, high-order accuracy (for smooth problems), high parallel efficiency, high processor efficiency,
51 and geometric flexibility facilitating mesh-refinement applications. NCAR’s Community Atmo-
52 sphere Model (CAM; Neale et al. 2012) offers a dynamical core based on continuous Galerkin
53 finite elements (Taylor and Fournier 2010), referred to as CAM-SE (CAM Spectral Elements;
54 Taylor et al. 2008; Dennis et al. 2012; Lauritzen et al. 2018). CAM-SE is, in particular, being used
55 for high resolution climate modeling (e.g., Small et al. 2014; Reed et al. 2015; Bacmeister et al.
56 2018) and static mesh-refinement applications (e.g., Fournier et al. 2004; Zarzycki et al. 2014a,b;
57 Guba et al. 2014b; Rhoades et al. 2016). Other examples of models based on high-order Galerkin
58 methods that are being considered for ‘operational’ weather-climate applications are Giraldo and
59 Restelli (2008), Nair et al. (2009), Brdar et al. (2013) and E3SM (<https://e3sm.org/>).

60 Assumptions inherent to the physical parameterizations (also referred to as *physics*) require
61 the state passed by the dynamical core represent a ‘large-scale state’, for example, in quasi-
62 equilibrium-type convection schemes (Arakawa and Schubert 1974; Plant 2008). In finite-volume
63 methods (e.g., Lin 2004), one may think of the dynamical core state as the average state of the
64 atmosphere over a control volume, and for resolutions typical of climate simulations is entirely
65 consistent with the notion of a ‘large-scale state’. For finite-difference methods (e.g., Suarez et al.

66 1983) the point value is thought of as representative for the atmospheric state in the vicinity of the
67 point value and one can usually associate a volume with the grid-point. Hence the physics grid (the
68 grid on which the state of the atmosphere is evaluated and passed to physics) and the dynamics
69 grid (the grid the dynamical core uses) coincide. Having the physics and dynamics grids coin-
70 cide is obviously convenient since no interpolation is needed (which could disrupt conservation
71 properties) and the number of degrees of freedom on both grids is exactly the same.

72 For the regular latitude-longitude, cubed-sphere and icosahedral grids the distance between the
73 grid-points is gradually varying for finite-volume/finite-difference discretizations. Examples of
74 models that use these grids are CAM-FV (latitude-longitude grid, Lin 2004), FV3 (cubed-sphere
75 grid, Putman and Lin 2007) and ICON (icosahedral grid, Wan et al. 2013). For high-order
76 element-based Galerkin methods, the dynamical core grid is defined by the quadrature points. In
77 CAM-SE, these are the Gauss-Lobatto-Legendre (GLL) quadrature nodes. A unique aspect of the
78 high-order quadrature rules is that the nodes within an element are located at the roots of the basis
79 set, which may be irregularly spaced. For example, Figure 1 shows GLL points on an individual
80 element of a cubed-sphere grid for degree 3 ($np \times np = 4 \times 4$ quadrature points) and degree 7
81 ($np \times np = 8 \times 8$ quadrature points) Lagrange polynomial basis used in CAM-SE. The higher
82 the order of the quadrature rule, the greater variance in distance between GLL quadrature points
83 within an element. GLL quadrature points cluster near the edges and, in particular, the corners of
84 the elements.

85 The resolved scales of motion are not determined by the distance between quadrature nodes,
86 but rather the degree of the polynomial basis in each element. The nodes may be viewed as
87 irregularly spaced samples of an underlying spectrally truncated state. From this perspective, one
88 might expect the nodal solutions to be independent of location within an element. While the
89 interior quadrature nodes are C^∞ in CAM-SE (i.e. the basis representation is infinitely smooth

and all derivatives are continuous), the smoothness of boundary nodes are constrained by the need to patch neighboring solutions together to form the global basis set, an operation known as the direct stiffness summation (DSS; Maday and Patera 1987; Canuto et al. 2007). The DSS operation is attractive because it allows for high-order accuracy with minimal communication between elements, but degrades the solution to C^0 at element boundaries (i.e., all derivatives are discontinuous). Through evaluating the physics at the nodal points, strong grid-scale forcing or oscillatory behavior near an element boundary may exacerbate the discontinuity, and our initial expectation, that the nodal solutions are independent of within-element location, is unlikely for non-smooth problems, e.g., the presence of rough topography or moist physics grid-scale forcing.

It is the purpose of this paper to document the implementation of an entirely separate, quasi-equal area finite-volume physics grid into CAM-SE. In this framework, the dynamical core state is integrated over control volumes to provide a volume averaged state to the physics, thereby minimizing the influence of any one particular nodal value on the physics forcing. Section 2 provides a thorough explanation of how grid imprinting manifests in high-order Galerkin methods for non-smooth problems. The implementation of the physics grid configuration into CAM-SE is presented in Section 3. Results from a hierarchy of idealized model configurations are presented in Section 4, illustrating the physics grid is effective at mitigating undesirable grid imprinting in the solution. Section 5 contains a discussion of results and concluding remarks.

2. The Quadrature Node Problem

Figure 2 is a schematic illustrating in one-dimension how grid-imprinting is enabled by the physics, when the dynamical core is built using high-order Galerkin methods. The schematic depicts a time-step, starting from smooth initial conditions (Figure 2a), and subsequently advancing the dynamics one Runge-Kutta time-step (Figure 2b). Since the boundary nodes of adjacent

elements overlap one-another, there are now two solutions for each boundary node. The DSS operator, effectively a numerical flux applied to the element boundaries such that overlapping nodal values agree, is applied (Figure 2c), degrading the boundary nodes to C^0 in the process. This discontinuity may be exacerbated if, e.g., the physics updates the state at an element boundary (Figure 2d,e), resulting in characteristically tighter gradients on the boundary nodes compared to if the physics forcing were applied to an interior node (Figure 2g,h).

To test the degree to which nodal solutions depend on within-element position, an aqua-planet simulation (Neale and Hoskins 2000; Medeiros et al. 2016), which consists of an ocean covered planet in perpetual equinox, with fixed, zonally symmetric sea surface temperatures idealized after the present day climatology, is carried out using CAM-SE, using CAM, version 4 physics (CAM4; Neale et al. 2010) and run for one year. The nominal low resolution *ne30np4* grid is used, pertaining to an average equatorial grid spacing of 111.2km. The probability density distribution of the upward vertical pressure velocity (ω), conditionally sampled based on three categories - ‘interior’, ‘edge’ and ‘corner’ nodes - is provided in Figure 3a. The rationale for concentrating on the ω field is that it closely follows divergent modes, which are sensitive to the discontinuous pressure gradients that characterize boundary nodes. There is an apparent dependence on nodal location, with interior nodes being characteristically sluggish, and corner and edge nodes having systematically larger magnitude vertical motion. This behavior is consistent with the smoothness properties of the different nodal locations, with discontinuous pressure gradients resulting in greater vertical motion at edge and corner nodes. The main division of solutions shown in Figure 3a is primarily between whether a node is, or is not situated on an element boundary, and is a nuanced signature of high-order element-based Galerkin methods for non-smooth problems.

If the conventional physics-dynamics coupling paradigm is applied to CAM-SE, then the physics are to be evaluated at the GLL nodes, and a volume associated with the quadrature point should

be defined. One approach to construct this grid is to decompose each spectral element into $(np - 1) \times (np - 1)$ subcells and then take the dual grid of this subcell grid. For cubed-sphere meshes, this dual grid will have a control volume associated with each quadrature point. These control volumes will be triangles for the cube corner quadrature points and quadrilaterals for all remaining quadrature points. Newton iteration can then be used to adjust the corners of these control volumes so that their spherical area exactly match the Gaussian weight multiplied by the metric term (these weights are used for integrating the basis functions over the elements and can therefore, in this context, be interpreted as areas). For cubed-sphere meshes, the Newton iteration can be replaced by a direct method if some of the quadrilaterals are replaced by pentagons giving additional flexibility in matching the spherical area to the quadrature weights. Such a dual grid is shown in Figure 4. This grid is used in the NCAR CESM (Community Earth System Model) coupler for passing states between ocean, atmosphere and land components since the current remapping method is finite-volume based and therefore requires control volumes (it is noted that methods exist that do not require control volumes for conservative interpolation, e.g., Ullrich and Taylor (2015)). Hence the components ‘see’ an irregular atmospheric grid. Similarly, the parameterizations in the atmosphere ‘see’ a state that is anisotropically sampled in space (see Figure 1 and 5 in Kim et al. 2008).

The quadrature grid in element-based Galerkin methods is defined to perform mathematical operations on the basis functions, e.g., computing gradients and integrals, rather than evaluating the state variables for physics-dynamics coupling. One may argue that it would be more consistent to integrate the basis functions over quasi-equal area control volumes within each element and pass those control volume average values to physics rather than irregularly spaced quadrature point values. In this case when integrating basis functions over control volumes a grid-cell average value is more representative of the values near the extrema at the element boundary than the quadrature

161 point value. The relationship between the nodal values, the basis functions and the proposed
162 control volumes is illustrated schematically in one-dimension in parts (f) and (i) in Figure 2.

163 **3. Methods**

164 Here we focus on CAM-SE, however, in principle the methods apply to any element-based high-
165 order Galerkin model. The physics grid in CAM-SE is defined by sub-dividing each element using
166 equi-angular gnomonic coordinate lines to define the sides of the physics grid control volumes (see
167 the Appendix for details). Note that the element boundaries are defined by equi-angular gnomonic
168 grid lines. The notation $pg = 3$ refers to the configuration where the elements are divided into
169 $pg \times pg = 3 \times 3$ equi-angular physics grid cells (see Figure 5) **resulting in a quasi-equal spherical**
170 **area grid resembling the cubed-sphere**. Defining the physics grid by sub-dividing elements makes
171 it possible to use the same element infrastructure as already used in CAM-SE, thereby facilitating
172 its implementation. Here we make use of the *ne30np4* and *ne30pg3* grids that use GLL quadrature
173 point physics grid (physics and dynamics grid coincide), and the same ($pg = 3$) resolution quasi-
174 equal-area physics grids, respectively. In all configurations we use degree three Lagrange basis
175 ($np = 4$) and $ne \times ne = 30 \times 30$ elements on each cubed-sphere panel.

176 A consequence of separating physics and dynamics grids is that the atmospheric state must be
177 mapped to the physics grid and the physics tendencies must be mapped back to the dynamics
178 grid. This is discussed in separate sections below. When separating physics and dynamics grids it
179 is advantageous to use a vertical coordinate that is static during physics-dynamics coupling. This
180 was one motivation to switch to a dry-mass vertical coordinate in CAM-SE (Lauritzen et al. 2018);
181 since dry mass remains constant throughout physics the dry-mass vertical coordinate remains fixed
182 during physics-dynamics coupling. **The dry mass coordinate subsequently evolves as floating**
183 **Lagrangian layers by the dynamics (Lin 2004) periodically mapped back to a reference hybrid-**

184 sigma-pressure coordinate after Simmons and Burridge (1981). All variables mapped between
185 grids are collocated, layer-mean values (Lauritzen et al. 2018).

186 *a. Mapping state from dynamics grid (GLL) to physics grid (pg)*

187 The dynamics state is defined on the GLL grid in terms of temperature $T^{(gll)}$, zonal wind com-
188 ponent $u^{(gll)}$, meridional wind component $v^{(gll)}$, and dry pressure level thickness $\Delta p^{(gll)}$. In the
189 mapping of the atmospheric state to the physics grid it is important that the following properties
190 are met:

- 191 1. conservation of scalar quantities such as mass and dry thermal energy,
- 192 2. for tracers; shape-preservation (monotonicity), i.e. the mapping method must not introduce
193 new extrema in the interpolated field, in particular, negatives,
- 194 3. consistency, i.e. the mapping preserves a constant,
- 195 4. linear correlation preservation.

196 Other properties that may be important, but not pursued here, includes total energy conservation
197 and axial angular momentum conservation; the main reason being that we did not manage to
198 construct a high-order reversible map that is consistent, shape-preserving and conservative. Also,
199 enforcing total energy conservation locally using, e.g. Lin (2004)'s method where total energy and
200 velocity components are remapped and temperature is a derived variable, has proven problematic
201 (C. Chen, personal communication).

202 We argue that the most consistent method for mapping scalar state variables from the GLL grid
203 to the physics grid is to integrate the Lagrange basis function representation (used by the SE dy-
204 namical core) over the physics grid control volumes, i.e. integrate the basis function representation
205 of $\Delta p^{(gll)} \times T^{(gll)}$ and $\Delta p^{(gll)}$ over the physics grid control volume (see, e.g., Lauritzen et al. 2017;

$$\Delta p^{(pg)} = \frac{1}{A^{(pg)}} \int_{A^{(pg)}} \Delta p^{(gll)} dA, \quad (1)$$

$$T^{(pg)} = \frac{1}{A^{(pg)} \Delta p^{(pg)}} \int_{A^{(pg)}} T^{(gll)} \Delta p^{(gll)} dA, \quad (2)$$

207 where $A^{(pg)}$ is the physics grid area. The integrals are numerically computed using the GLL
 208 quadrature rule which exactly (to machine precision) integrates the basis functions over the pg
 209 control volumes (Lauritzen et al. 2017). Thermal energy and dry air mass is conserved and the
 210 mapping is consistent. For the wind, which is a vector, the zonal and meridional wind components
 211 are mapped by transforming to contra-variant wind components, evaluating the basis function
 212 representation thereof at the equi-angular center of the physics grid control volumes and then
 213 transformed back to latitude-longitude coordinate system winds. All of the operations are local to
 214 the element and do not require communication between elements.

215 The mapping of tracers is more problematic since the SE basis function representation is oscil-
 216 latory although the shape-preserving filter guarantees shape-preservation at the GLL nodes (Guba
 217 et al. 2014a). To avoid this issue we use the CAM-SE-CSLAM version of CAM-SE (Conservative
 218 Semi-Lagrangian Multi-tracer transport scheme Lauritzen et al. 2017), where tracers are advected
 219 on the $pg = 3$ physics grid. Note that in CAM-SE-CSLAM the dry mass internally predicted by
 220 CSLAM, $\Delta p^{(cslam)}$, is, by design, equal to $\Delta p^{(gll)}$ integrated over the CSLAM/physics grid con-
 221 trol volume (Lauritzen et al. 2017). Since the tracer grid and physics grids are co-located and
 222 $\Delta p^{(pg)} = \Delta p^{(cslam)}$ then the mass conservation, correlation preservation, consistency and shape-
 223 preservation constraints are inherently fulfilled.

224 b. *Mapping tendencies from physics grid (pg) to dynamics grid (GLL)*

225 The physics tendencies are computed on the finite-volume physics grid and are denoted
226 $f_T^{(pg)}, f_u^{(pg)}, f_v^{(pg)}$, and $f_m^{(pg)}$. Note that dry air mass is not modified by physics and hence there
227 is no tendency for dry mass, $f_{\Delta p} \equiv 0$. Also, it is important to map tendencies and not state from
228 the physics grid to GLL grid otherwise one will get spurious tendencies from mapping errors when
229 the actual physics tendency is zero (unless a reversible map is used).

230 It is important that this process:

231 1. for tracers; mass tendency is conserved,

232 2. for tracers; in each tracer grid cell the mass tendency from physics must not exceed tracer
233 mass available in tracer grid cell (it is assumed that the physics tendency will not drive tracer
234 mixing ratio negative on the physics grid),

235 3. linear correlation preservation,

236 4. consistency, i.e. the mapping preserves a constant tendency.

237 Other properties that may be important, but not pursued here, includes total energy conservation
238 (incl. components of total energy) and axial angular momentum conservation. Scalar variables
239 are mapped from **the** physics grid to GLL grid using a tensor-product Lagrange interpolation **in**
240 **two dimensions (i.e. we assume that the pressure variations in the vertical are small)**. The local
241 coordinates on a cubed-sphere are discontinuous at the element edges so the interpolation requires
242 special attention at the cube corners and edges. The details are provided in the Appendix. Lagrange
243 interpolation preserves a constant (including zero) and linear correlations. Tracer and physics grids
244 are co-located so tracer mass, tracer shape, and tracer correlations are trivially preserved on the
245 tracer grid; and the inconsistency in point 2 above will not appear.

246 Mapping from pg to GLL grids while conserving mass was found to be difficult without ex-
247 cessive grid imprinting at element edges. Mass-conservation (using conventional finite-volume
248 methods) requires a control volume to be defined around the GLL points (see, .e.g., Figure 4 in
249 this paper or Figure 8b in Ullrich et al. 2016). These volumes are artificial and not consistent with
250 the SE method. Integrating the CSLAM reconstruction of water tracers of such artificial control
251 volumes led to GLL node grid imprinting in the mapping and will not preserve a constant mixing
252 ratio since the mapping of $\Delta p^{(pg)}$ to GLL will not yield the GLL node value for dry pressure-level
253 thickness (i.e. the maps are not reversible).

254 It was also found important to use an interpolator that is smooth across element boundaries.
255 Using an algorithm that only uses information from an element of control volumes will (at best)
256 be C^0 at the element boundaries and therefore lead to boundary node grid imprinting. A stencil
257 that extends beyond one element is therefore necessary. After much experimentation, the best
258 results in terms of grid-imprinting were obtained with tensor-cubic interpolation and by using the
259 CAM-SE-CSLAM configuration (which requires the same boundary exchange/communication as
260 used in CSLAM).

261 *c. Time splitting and physics-dynamics coupling*

262 The physics and dynamics are integrated in time using a sequential-update approach (e.g.,
263 Williamson 2002). The dynamical core is sub-cycled over the (usually) longer physics time-step,
264 Δt_{phys} , e.g., the vertical remapping time-step Δt_{remap} is cycled $rsplit$ times, totaling to Δt_{phys} . In
265 CAM-SE, a fraction of the physics forcing, e.g., $f_q \times \Delta t_{remap}$ is applied at the beginning of each
266 $rsplit$ vertical remap subcycles, such that the full forcing ($f_q \times \Delta t_{phys}$) is realized over the course
267 of a physics time-step. This approach of dribbling the tendencies over sub-intervals has the ad-
268 vantage of reducing gravity wave noise (Thatcher and Jablonowski 2016), but may disrupt tracer

269 mass conservation (Zhang et al. 2017). In CAM-SE-CSLAM, all but the tracer mass quantities are
270 dribbled, with tracer mass receiving the full physics update, e.g., $f_q \times \Delta t_{phys}$, applied only at the
271 beginning of the first remap sub-cycle, and thereby conserving tracer mass. This is the $f_{type} = 2$
272 configuration described in detail in Section 3.6.3 in Lauritzen et al. (2018).

273 In the SE integration of the equations of motion on the GLL grid the water species are
274 needed in the computation of the pressure gradient force and generalized expressions for heat
275 capacity at constant pressure c_p , etc. Hence the mixing ratios for water vapor and dynamical-
276 thermodynamically active condensates (e.g., cloud ice, cloud liquid) are needed on the GLL
277 grid. We have chosen to advect the water species on the GLL grid using the SE method as well as
278 on the physics grid using CSLAM. Every time physics updates the water species on the CSLAM
279 grid, a forcing term (equal to the difference between updated CSLAM water variables and the SE
280 values) is applied to the GLL water variables using dribbling so that the CSLAM solution and SE
281 solution for water species are tightly coupled.

282 4. Results

283 A hierarchy of idealized model configurations are presented in order to elucidate the differ-
284 ences between CAM-SE and CAM-SE-CSLAM (available from the CESM2.1 release; <https://doi.org/10.5065/D67H1H0V>). Here, the configurations are presented in order of increas-
285 ing complexity, each with a pair of approximately 1° simulations, pertaining to the *ne30np4* and
286 *ne30pg3* grids, and a $\Delta t_{phys} = 1800$ s.
287

288 a. *Moist Baroclinic Wave*

289 The moist baroclinic wave test case was developed as part of the ‘CESM Simple Models’ project
290 (Polvani et al. 2017), and included in the release of CESM2. It is effectively the dry test-case of

291 Ullrich et al. (2014), but initialized with moisture and coupled to the Kessler moist physics routine
292 (Kessler 1969). For more details on this test case (which was part of the 2016 Dynamical Core
293 Model Intercomparison Project, see Ullrich et al. 2017), see Section 4.1 in Lauritzen et al. (2018).
294 A measure of the uncertainty of the reference solution, the L_2 difference norm between two high-
295 resolution solutions using different dynamical cores, was also presented in Lauritzen et al. (2018)
296 and provided again here in Figure 6. The L_2 norm between CAM-SE and CAM-SE-CSLAM lies
297 below the uncertainty of the reference solution, indicating their differences are insignificant.

298 The flow field of the baroclinic wave test is used to drive the terminator "toy"-chemistry test of
299 Lauritzen et al. (2015b). The terminator test is used to assess the tracer mass conservation prop-
300 erties for linear-correlated reactive species being advected across the terminator line. The model
301 is initialized with two species for which their total mass is constant everywhere (constant surface
302 pressure and constant mixing ratio 4×10^{-6} kg/kg), such that if tracer mass is conserved, then the
303 columns mass weighted sum of the species should not vary in time. Figure 7 provides a snap-
304 shot of the mass-weighted, vertically integrated tracer concentration at day 15. In CAM-SE, the
305 tracer mass is not conserved by day 15 and the field is populated by overshoots and undershoots.
306 In contrast, by day 15, CAM-SE-CSLAM still conserves tracer mass to within machine preci-
307 sion, consistent with the previous results of this test-case initialized with a dry baroclinic wave
308 (Lauritzen et al. 2017).

309 *b. Aqua-planets*

310 Two year long aqua-planet simulations are performed using CAM-SE and CAM-SE-CSLAM,
311 using the CAM4 physics package (Neale et al. 2010), as discussed in Section 2. Away from the
312 grid-scale, the mean states in the two models are very similar. Figure 8 shows the zonal-mean cli-
313 matological precipitation rates in CAM-SE and CAM-SE-CSLAM. Considering how sensitive this

314 aqua-planet configuration is to design choices in CAM-SE (Lauritzen et al. 2018), it is somewhat
315 unexpected that the zonal means look so similar to one another.

316 A plot similar to Figure 3a is constructed for the CAM-SE-CSLAM simulation, a probability
317 density distribution of upward ω conditionally sampled based on location within the element. Like
318 Figure 3a, Figure 3b divides up the control volumes by corner, edge and interior cells. Through the
319 use of the quasi-equal area physics grid, the dynamical core state appears more or less independent
320 of location within the element, a marked improvement over CAM-SE. Since the state is approxi-
321 mately independent of in-element location, it follows that the physics forcing, which is evaluated
322 from the dynamical core state, may be expected to also show an improvement in grid-imprinting.

323 The low-level, mean and variance of the temperature tendencies from the physics in the two sim-
324 ulations are shown in Figure 9. The mean states in the two models resemble one another, consistent
325 with the zonal mean precipitaiton rates (Figure 8). The mean physics tendencies contains modest
326 grid imprinting in CAM-SE (barely visible near the storm-track regions), while in the variance
327 field, grid imprinting is both ubiquitous and unmistakable. The variance is larger on boundary
328 nodes, manifesting as a ‘stitching’ pattern resembling the cube-sphere grid. In CAM-SE-CSLAM,
329 the grid imprinting is all but eliminated based on the mean and variance of the physics tendencies
330 (Figure 9), consistent with our expectation.

331 As stated in Section 3, the mapping of the state to the physics grid and the reverse interpolation
332 of physics tendencies to the GLL grid is not total energy conserving. CAM has a global energy
333 fixer (Williamson et al. 2015) which can be used to estimate the errors associated with the mapping
334 algorithms. To do so, it is presumed that there are no compensating mapping errors in going to
335 and from the physics and dynamics grids, and that CAM-SE-CSLAM and CAM-SE have the same
336 energy dissipation rates. Under these assumptions the spurious globally integrated total energy
337 errors due to the mapping algorithm is estimated to be approximately 0.0025 W/m^2 in the aqua-

338 planet simulations. In comparison, the dynamical core total energy dissipation is on the order of
339 0.1 W/m^2 (Lauritzen et al. 2018).

340 *c. Held-Suarez with Topography*

341 Grid imprinting associated with the flow around obstacles is more problematic than that en-
342 countered on the aqua-planets. In order to diagnose grid imprinting due to topographic flow, an
343 idealized Held-Suarez configuration (Held and Suarez 1994) is outfitted with real world topogra-
344 phy after Fox-Rabinovitz et al. (2000); Baer et al. (2006), and run for two years. Figure 10 shows
345 the mean ω at two different vertical levels in the middle troposphere. **The data are presented as a**
346 **raster plot on their respective unstructured grids, in order to delineate whether a particular value is**
347 **associated with an interior, edge or element boundary node.**

348 At higher latitudes (e.g., the southern Andes), the flow is smooth, conforming reasonably to the
349 underlying topography. At lower latitudes (within 20 to 30 degrees from the equator), over the
350 Andes or the Himalayas, there is a clear preference for extrema to occur at the element bound-
351 aries (Figure 10). The vertical structure of ω in regions of strong grid-imprinting indicates full-
352 troposphere upward/downward motion (not shown). Grid imprinting is therefore more common
353 in regions of weak stratification, such as occurs in the deep tropics, with forced up-slope flow
354 facilitating the release of gravitational instability. Resolved updrafts/downdrafts often align with
355 the element boundaries due to its systematically tighter pressure gradients.

356 Through the use of the quasi-equal area physics grid, grid imprinting due to topographic flow is
357 reduced (Figures 10). Figure 10 also shows the state in CAM-SE-CSLAM, but on the GLL grid.
358 Arguably, grid imprinting due to topography in CAM-SE-CSLAM is not much of an improvement
359 over CAM-SE, viewed from the GLL grid. The native topography lives on the physics grid, and the
360 topography is mapped to the nodal points at run-time in CAM-SE-CSLAM. Mapping topography

361 to the quadrature nodes ensures that no new extrema will be introduced to the boundary nodes,
362 where the solution is least smooth. This effect can not be very large, since the grid noise is similar
363 in CAM-SE and CAM-SE-CSLAM on the GLL grid. From the perspective of the physics grid,
364 the CAM-SE-CSLAM solution clearly mitigates the influence of grid-induced extrema on the state
365 (Figure 10). The reduction in grid imprinting in CAM-SE-CSLAM is therefore almost entirely a
366 result of the smoothing effect of integrating the basis functions over the control volumes of the
367 physics grid.

368 *d. AMIP type simulations*

369 A pair of 20 year-long AMIP type simulations are performed, using CAM, version 6 physics
370 package (CAM6) and using perpetual year 2000 SST boundary conditions (*F2000climo* compset
371 in CESM2.0; <https://doi.org/10.5065/D67H1H0V>). Figure 11 shows the climatological pre-
372 cipitation fields in CAM-SE (left) and CAM-SE-CSLAM (middle), and over the same mountain-
373 ous regions as in Figure 10. The plots have some similar features to the ω field in the Held-Suarez
374 runs; the greater variance at lower latitudes, and on the windward side of the mountains are broadly
375 similar. CAM-SE-CSLAM has a lower spatial variance, e.g., the lack of extrema over the Andes
376 at about 15° S compared to CAM-SE, and the grid-scale precipitation peak over the Himalayas
377 at about 30° N. The difference plot (Figure 11; right panel) is more broadly populated by blue,
378 purple and white contours, indicating that CAM-SE has, in general, lower magnitude precipitation
379 rates over high topography. The difference plots also highlight a couple of zonally aligned strips
380 of anomalous precipitation, in particular, near the foot of the Himalayas in CAM-SE. These bands
381 are in the same location as the bands of precipitation identified in CAM-SE in Lauritzen et al.
382 (2015a) (their Figure 7), but using CAM, version 5 physics, of which they argue are spurious in
383 nature.

384 To assist in identifying whether a particular precipitation pattern is spurious, an AMIP type sim-
385 ulation is carried out using the finite-volume dynamical core that uses a regular latitude-longitude
386 $0.9^\circ \times 1.25^\circ$ grid (CAM-FV; Neale et al. 2012). CAM-FV is the default low resolution model in
387 CESM2.0, and with its smoothly varying grid, does not suffer from the Quadrature Node Problem.
388 Figure 12 shows the global precipitation fields in CAM-SE, CAM-SE-CSLAM and CAM-FV,
389 compared to an observational dataset, the GPCP (1979-2003) gridded dataset (Huffman et al.
390 2001). The magnitude of the precipitation rates in all three models are higher than the GPCP
391 dataset (note the lack of red contours in the GPCP dataset), which should be interpreted cautiously
392 due to widely-accepted issues in constructing a reliable, gridded, global precipitation dataset. At
393 lower latitudes, CAM-FV has lower spatial variance, and overall lower magnitudes, compared
394 with CAM-SE. The GPCP dataset indicates that perhaps the precipitation rates in low-latitude
395 mountainous regions in CAM-FV and CAM-SE are larger than in reality. Following suit, the
396 reduction in magnitude and spatial variance in precipitation in these regions CAM-SE-CSLAM
397 may be interpreted as an improvement over CAM-SE and CAM-FV.

398 5. Conclusions

399 Element-based high-order Galerkin Methods possess many of the attractive qualities recom-
400 mended for next generation global atmospheric models. Among these, high-order accuracy is
401 achieved with minimal communication between elements, allowing for near perfect scaling on
402 massively parallel systems. Element communication amounts to a numerical flux applied to the
403 element boundaries, reconciling overlapping solutions of adjacent elements but degrading the
404 smoothness of the boundary nodes in the process (to C^0). For non-smooth problems, gradients are
405 systematically tighter at the element boundaries, and local extrema often characterize the boundary
406 nodes. This behavior is illustrated using NCAR’s Community Atmosphere Model with Spectral

407 Elements dynamics (CAM-SE) in an aqua-planet configuration, in a Held-Suarez configuration
408 with real-world topography **and in an AMIP type configuration.**

409 The authors argue that the conventional physics-dynamics coupling paradigm, in which the
410 physical parameterizations are evaluated on the dynamical core grid, exacerbates grid imprinting.

411 A separate physics grid is proposed and implemented in CAM-SE, and referred to as CAM-SE-
412 CSLAM, through dividing the elements into quasi-equal areas with equivalent degrees of freedom.

413 The state is mapped to the physics grid with high-order accuracy through integrating CAM-SE's
414 Lagrange basis functions over the control volumes. Control volumes near element boundaries now

415 represent a state in the vicinity of the extrema produced through the boundary exchange, as op-
416 posed to the the nodal value itself. These control volumes are also compatible with a 'large-scale

417 state' as required by the physical parameterizations. The physical parameterizations are evalu-
418 ated on the finite volume grid, and the forcing terms are mapped back to the dynamical core grid

419 using a cubic tensor-product Lagrange interpolation. In aqua-planet simulations, evaluating the
420 parameterizations on the physics grid removes any obvious dependence of proximity to the ele-

421 ment boundary, resulting in a more realistic state with negligible grid imprinting. The mapping
422 algorithm does not conserve total energy, but it is estimated that these errors are one to two orders
423 of magnitude less than the total energy dissipation from the dynamical core.

424 In CAM-SE-CSLAM, the physics grid replaces the default CAM-SE quadrature point-based
425 coupler grid (Figure 4) to compute fluxes between model components in the Community Earth

426 System Model (CESM). The appeal here is two-fold. Through integrating the Lagrange basis
427 functions over control volumes, one can be certain that the fluxes computed from this grid are
428 a volume averaged flux. The same can not be said for CAM-SE, where the nodal values are

429 effectively assigned to each control volume. The second advantage of the new coupler grid is
430 that extrema occurring on boundary nodes may no longer influence other model components, in

431 simulations without rough topography. While grid imprinting is effectively eliminated in the aqua-
432 planets, experiments with real-world topography (Held-Suarez and AMIP type configurations)
433 reduces, but does not entirely eliminate, imprinting from the mean state. The quasi-equal area
434 physics grid is nonetheless effective at mitigating numerical nuances associated with high-order
435 element-based Galerkin methods, for non-smooth problems.

436 *Acknowledgments.* NCAR is sponsored by the National Science Foundation (NSF). We thank
437 three anonymous reviewers for their helpful comments that significantly improved the clarity of
438 the manuscript. Herrington thanks NCAR’s Computational and Information Systems Laboratory
439 (CISL) and NCAR’s Climate and Global Dynamics division (CGD) for computational resources
440 and technical support. Herrington, Reed, and Lauritzen are grateful to the NCAR Advanced Study
441 Program graduate visitor program for funding Herrington’s 12-month visit. Goldhaber was par-
442 tially supported by the Accelerated Climate Modeling for Energy (ACME) project, and work pack-
443 age 12 – 015334 “Multiscale Methods for Accurate, Efficient, and the Accelerated Scale-Aware
444 Models, both funded through the U.S. Department of Energy Office of Biological and Environ-
445 mental Resarch. Goldhaber is also partially supported through NSF award AGS-1500187 “De-
446 velopment and Testing of a Global Quasi 3-D multi Modeling Framework.” Model source code is
447 officially released with CESM2.1 (<https://doi.org/10.5065/D67H1H0V>).

448 APPENDIX

449 The mapping of the physics tendencies from the physics grid to the GLL grid is done with
450 tensor-cubic Lagrange interpolation. The elements of the cubed-sphere in SE are created
451 from an equi-angular gnomonic projection. Consider one element $(\alpha, \beta) \in [\alpha_1^{(elem)}, \alpha_2^{(elem)}] \times$
452 $[\beta_1^{(elem)}, \beta_2^{(elem)}]$, where (α, β) are central angle coordinates and $\alpha_1^{(elem)}$ and $\alpha_2^{(elem)}$ are the min-
453 imum and maximum central angles in the α -coordinate direction, respectively, and similarly for

⁴⁵⁴ β . Let $\Delta\alpha^{(elem)} = \alpha_2^{(elem)} - \alpha_1^{(elem)}$ and $\Delta\beta^{(elem)} = \beta_2^{(elem)} - \beta_1^{(elem)}$. The physics grid cell central
⁴⁵⁵ angle centers are located at

$$(\alpha_i^{(pg)}, \beta_j^{(pg)}) = \left[\alpha_1^{(elem)} + (i - \frac{1}{2}) \Delta\alpha^{(pg)}, \right. \\ \left. \beta_1^{(elem)} + (j - \frac{1}{2}) \Delta\beta^{(pg)} \right], \quad (\text{A1})$$

⁴⁵⁶ where $\Delta\alpha^{(pg)} = \Delta\beta^{(pg)} = \frac{\Delta\alpha^{(elem)}}{pg} = \frac{\Delta\beta^{(elem)}}{pg}$. The interpolation is performed in central-angle co-
⁴⁵⁷ ordinates using tensor product cubic interpolation. For elements located on a cubed-sphere edge
⁴⁵⁸ or corner the coordinate system for neighboring elements may be on a different panel. To take
⁴⁵⁹ into account this coordinate change the central angle locations of physics grid cell centers located
⁴⁶⁰ on other panels are transformed to the coordinate system of the panel the element in question is
⁴⁶¹ located on (the transformations are given in, e.g., Nair et al. 2005). An illustration is given in
⁴⁶² Figure 13 for an element located in the lower left corner of a panel. The element in question is
⁴⁶³ $(\xi, \chi) \in (-1, 1)^2$ where, for simplicity, we have transformed the element coordinates into normal-
⁴⁶⁴ ized coordinates $(\xi, \chi) = \left(\frac{2(\alpha^{(pg)} - \alpha_1^{(elem)})}{\Delta\alpha^{(elem)}} - 1, \frac{2(\beta^{(pg)} - \beta_1^{(elem)})}{\Delta\beta^{(elem)}} - 1 \right)$; also used internally in the
⁴⁶⁵ SE dynamical core (see, e.g., section 3.3 in Lauritzen et al. 2018). The GLL points are located at
⁴⁶⁶ $-1, -1/\sqrt{1}, 1/\sqrt{5}$, and 1 in each coordinate direction. Near the edges/corners of an element cubic
⁴⁶⁷ extrapolation is used if the centered stencil expands beyond the panel.

⁴⁶⁸ References

- ⁴⁶⁹ Arakawa, A., and W. H. Schubert, 1974: Interaction of a cumulus cloud ensemble with the large-
⁴⁷⁰ scale environment, Part I. *J. Atmos. Sci.*, **31**, 674–701.
- ⁴⁷¹ Bacmeister, J. T., K. A. Reed, C. Hannay, P. Lawrence, S. Bates, J. E. Truesdale, N. Rosen-
⁴⁷² bloom, and M. Levy, 2018: Projected changes in tropical cyclone activity under future warm-

- 473 ing scenarios using a high-resolution climate model. *Climatic Change*, **146**, 547–560, doi:
474 10.1007/s10584-016-1750-x, URL <http://dx.doi.org/10.1007/s10584-016-1750-x>.
- 475 Baer, F., H. Wang, J. J. Tribbia, and A. Fournier, 2006: Climate modeling with spectral elements.
476 *Mon. Wea. Rev.*, **134**, 3610–3624, doi:10.1175/MWR3360.1, URL <http://dx.doi.org/10.1175/MWR3360.1>.
- 477 Brdar, S., M. Baldauf, A. Dedner, and R. Klfkorn, 2013: Comparison of dynamical cores for
478 nwp models: comparison of cosmo and dune. *Theoretical and Computational Fluid Dynamics*,
479 **27 (3-4)**, 453–472, doi:10.1007/s00162-012-0264-z.
- 480 Canuto, C., M. Y. Hussaini, A. Quarteroni, and T. Zang, 2007: *Spectral Methods: Evolution to
481 Complex Geometries and Applications to Fluid Dynamics*. 1st ed., Springer.
- 482 Dennis, J. M., and Coauthors, 2012: CAM-SE: A scalable spectral element dynamical core for
483 the Community Atmosphere Model. *Int. J. High. Perform. C.*, **26 (1)**, 74–89, doi:10.1177/
484 1094342011428142, URL <http://hpc.sagepub.com/content/26/1/74.abstract>, <http://hpc.sagepub.com/content/26/1/74.full.pdf+html>.
- 485 Durran, D., 2010: *Numerical Methods for Fluid Dynamics: With Applications to Geophysics*,
486 Texts in Applied Mathematics, Vol. 32. 2nd ed., Springer, 516 p.
- 487 Fournier, A., M. A. Taylor, and J. J. Tribbia, 2004: The spectral element atmosphere model
488 (SEAM): High-resolution parallel computation and localized resolution of regional dynamics.
489 *Mon. Wea. Rev.*, **132 (3)**, 726–748.
- 490 Fox-Rabinovitz, M. S., G. L. Stenchikov, M. J. Suarez, L. L. Takacs, and R. C. Govindaraju, 2000:
491 A uniform- and variable-resolution stretched-grid gcm dynamical core with realistic orography.
492 *Mon. Wea. Rev.*, **128**, 1883–1898.

- 495 Giraldo, F., and M. Restelli, 2008: A study of spectral element and discontinuous galerkin methods
496 for the Navier-Stokes equations in nonhydrostatic mesoscale atmospheric modeling: Equation
497 sets and test cases. *J. Comput. Phys.*, **227** (8), 3849 – 3877, doi:<http://dx.doi.org/10.1016/j.jcp>.
498 2007.12.009.
- 499 Guba, O., M. Taylor, and A. St-Cyr, 2014a: Optimization-based limiters for the spectral element
500 method. *J. Comput. Phys.*, **267** (0), 176 – 195, doi:<http://dx.doi.org/10.1016/j.jcp.2014.02.029>.
- 501 Guba, O., M. A. Taylor, P. A. Ullrich, J. R. Overfelt, and M. N. Levy, 2014b: The spectral element
502 method (sem) on variable-resolution grids: evaluating grid sensitivity and resolution-aware nu-
503 matical viscosity. *Geosci. Model Dev.*, **7** (6), 2803–2816, doi:[10.5194/gmd-7-2803-2014](https://doi.org/10.5194/gmd-7-2803-2014).
- 504 Held, I. M., and M. J. Suarez, 1994: A proposal for the intercomparison of the dynamical cores of
505 atmospheric general circulation models. *Bull. Am. Meteorol. Soc.*, **73**, 1825–1830.
- 506 Huffman, G. J., R. F. Adler, M. M. Morrissey, D. T. Bolvin, S. Curtis, R. Joyce, B. McGavock,
507 and J. Susskind, 2001: Global precipitation at one-degree daily resolution from multisatellite
508 observations. *J. Hydrometeorology*, **2** (1), 36–50.
- 509 Kessler, E., 1969: On the distribution and continuity of water substance in atmospheric circula-
510 tions. *Meteorol. Monogr.*, **10** (32), 88.
- 511 Kim, Y.-J., F. X. Giraldo, M. Flatau, C.-S. Liou, and M. S. Peng, 2008: A sensitivity study of the
512 kelvin wave and the Madden-Julian oscillation in aquaplanet simulations by the Naval Research
513 Laboratory Spectral Element Atmospheric Model. *J. Geo. Res.: Atmospheres*, **113** (D20), doi:
514 [10.1029/2008JD009887](https://doi.org/10.1029/2008JD009887), d20102.

- 515 Lauritzen, P. H., J. T. Bacmeister, P. F. Callaghan, and M. A. Taylor, 2015a: Ncar global model
516 topography generation software for unstructured grids. *Geoscientific Model Development Discussions*, **8 (6)**, 4623–4651, doi:10.5194/gmdd-8-4623-2015.
- 517
- 518 Lauritzen, P. H., A. J. Conley, J.-F. Lamarque, F. Vitt, and M. A. Taylor, 2015b: The terminator
519 “toy” chemistry test: a simple tool to assess errors in transport schemes. *Geoscientific Model
520 Development*, **8 (5)**, 1299–1313, doi:10.5194/gmd-8-1299-2015.
- 521 Lauritzen, P. H., M. A. Taylor, J. Overfelt, P. A. Ullrich, R. D. Nair, S. Goldhaber, and
522 R. Kelly, 2017: CAM-SE-CSLAM: Consistent coupling of a conservative semi-lagrangian
523 finite-volume method with spectral element dynamics. *Mon. Wea. Rev.*, **145 (3)**, 833–855, doi:
524 10.1175/MWR-D-16-0258.1.
- 525 Lauritzen, P. H., and Coauthors, 2018: Ncar cesm2.0 release of cam-se: A reformulation of the
526 spectral-element dynamical core in dry-mass vertical coordinates with comprehensive treatment
527 of condensates and energy. *J. Adv. Model. Earth Syst.*, doi:10.1029/2017MS001257.
- 528 Lin, S.-J., 2004: A ‘vertically Lagrangian’ finite-volume dynamical core for global models. *Mon.
529 Wea. Rev.*, **132**, 2293–2307.
- 530 Maday, Y., and A. T. Patera, 1987: Spectral element methods for the incompressible Navier Stokes
531 equations. *State of the Art Surveys on Computational Mechanics*, A. K. Noor, and J. T. Oden,
532 Eds., ASME, New York, 71–143.
- 533 Medeiros, B., D. L. Williamson, and J. G. Olson, 2016: Reference aquaplanet climate in the
534 community atmosphere model, version 5. *J. Adv. Model. Earth Syst.*, **8 (1)**, 406–424, doi:10.
535 1002/2015MS000593.

- 536 Nair, R., H.-W. Choi, and H. Tufo, 2009: Computational aspects of a scalable high-order dis-
537 continuous galerkin atmospheric dynamical core. *Computers & Fluids*, **38** (2), 309 – 319, doi:
538 <http://dx.doi.org/10.1016/j.compfluid.2008.04.006>.
- 539 Nair, R. D., M. N. Levy, and P. H. Lauritzen, 2011: Emerging numerical methods for atmo-
540 spheric modeling, in: P.H. Lauritzen, R.D. Nair, C. Jablonowski, M. Taylor (Eds.), Numerical
541 techniques for global atmospheric models. *Lecture Notes in Computational Science and Engi-
542 neering, Springer*, **80**.
- 543 Nair, R. D., S. J. Thomas, and R. D. Loft, 2005: A discontinuous galerkin transport scheme on the
544 cubed sphere. *Mon. Wea. Rev.*, **133** (4), 814–828, doi:10.1175/MWR2890.1.
- 545 Neale, R. B., and B. J. Hoskins, 2000: A standard test for agcms including their physical
546 parametrizations: I: the proposal. *Atmos. Sci. Lett.*, **1** (2), 101–107, doi:10.1006/asle.2000.0022.
- 547 Neale, R. B., and Coauthors, 2010: Description of the NCAR Community Atmosphere Model
548 (CAM 4.0). NCAR Technical Note, National Center of Atmospheric Research.
- 549 Neale, R. B., and Coauthors, 2012: Description of the NCAR Community Atmosphere Model
550 (CAM 5.0). NCAR Technical Note NCAR/TN-486+STR, National Center of Atmospheric Re-
551 search.
- 552 Plant, G. C. C., R. S., 2008: A stochastic parameterization for deep convection based on equilib-
553 rium statistics. *J. Atmos. Sci.*, **65**, 87–105, doi:10.1175/2007JAS2263.1, URL <http://dx.doi.org/10.1175/2007JAS2263.1>.
- 555 Polvani, L., A. Clement, B. Medeiros, J. Benedict, and I. Simpson, 2017: Opening the door to
556 simpler climate models in the community earth system model project. *EOS*, submitted.

- 557 Putman, W. M., and S.-J. Lin, 2007: Finite-volume transport on various cubed-sphere grids. *J.*
558 *Comput. Phys.*, **227** (1), 55–78.
- 559 Reed, K. A., J. T. Bacmeister, N. A. Rosenbloom, M. F. Wehner, S. C. Bates, P. H. Lauritzen,
560 J. E. Truesdale, and C. Hannay, 2015: Impact of the dynamical core on the direct simulation
561 of tropical cyclones in a high-resolution global model. *Geophys. Res. Lett.*, **42** (9), 3603–3608,
562 doi:10.1002/2015GL063974.
- 563 Rhoades, A. M., X. Huang, P. A. Ullrich, and C. M. Zarzycki, 2016: Characterizing sierra
564 nevada snowpack using variable-resolution cesm. *Journal of Applied Meteorology and Cli-*
565 *matology*, **55** (1), 173–196, doi:10.1175/JAMC-D-15-0156.1, URL <https://doi.org/10.1175/JAMC-D-15-0156.1>.
- 566
- 567 Simmons, A. J., and D. M. Burridge, 1981: An energy and angular-momentum conserving vertical
568 finite-difference scheme and hybrid vertical coordinates. *Mon. Wea. Rev.*, **109** (4), 758–766.
- 569
- 570 Small, R. J., and Coauthors, 2014: A new synoptic scale resolving global climate simulation using
571 the community earth system model. *Journal of Advances in Modeling Earth Systems*, **6** (4),
572 1065–1094, doi:10.1002/2014MS000363.
- 573
- 574 Suarez, M. J., A. Arakawa, and D. A. Randall, 1983: The parameterization of the planetary
575 boundary layer in the ucla general circulation model: Formulation and results. *Mon. Wea. Rev.*,
576 **111** (11), 2224–2243.
- 577
- 578 Taylor, M., J. Edwards, and A. St-Cyr, 2008: Petascale atmospheric models for the community
579 climate system model: new developments and evaluation of scalable dynamical cores. *J. Phys.:
580 Conf. Ser.*, **125**, doi:10.1088/1742-6596/125/1/012023.

- 578 Taylor, M. A., and A. Fournier, 2010: A compatible and conservative spectral element method on
579 unstructured grids. *J. Comput. Phys.*, **229** (17), 5879 – 5895, doi:10.1016/j.jcp.2010.04.008.
- 580 Thatcher, D. R., and C. Jablonowski, 2016: A moist aquaplanet variant of the Held–Suarez test
581 for atmospheric model dynamical cores. *Geoscientific Model Development*, **9** (4), 1263–1292,
582 doi:10.5194/gmd-9-1263-2016, URL <https://www.geosci-model-dev.net/9/1263/2016/>.
- 583 Ullrich, P. A., 2014: A global finite-element shallow-water model supporting continuous and dis-
584 continuous elements. *Geosci. Model Dev.*, **7** (6), 3017–3035, doi:10.5194/gmd-7-3017-2014.
- 585 Ullrich, P. A., D. Devendran, and H. Johansen, 2016: Arbitrary-order conservative and consistent
586 remapping and a theory of linear maps: Part ii. *Mon. Wea. Rev.*, **144** (4), 1529–1549, doi:
587 10.1175/MWR-D-15-0301.1.
- 588 Ullrich, P. A., T. Melvin, C. Jablonowski, and A. Staniforth, 2014: A proposed baroclinic wave test
589 case for deep and shallow-atmosphere dynamical cores. *Quart. J. Royal Meteor. Soc.*, **140** (682),
590 1590–1602.
- 591 Ullrich, P. A., and M. A. Taylor, 2015: Arbitrary-order conservative and consistent remap-
592 ping and a theory of linear maps: Part I. *Mon. Wea. Rev.*, **143**, 2419–2440, doi:10.1175/
593 MWR-D-14-00343.1.
- 594 Ullrich, P. A., and Coauthors, 2017: Dcmip2016: A review of non-hydrostatic dynamical core
595 design and intercomparison of participating models. *Geosci. Model Dev.*, **10**, 4477–4509, doi:
596 10.5194/gmd-10-4477-2017.
- 597 Wan, H., and Coauthors, 2013: The icon-1.2 hydrostatic atmospheric dynamical core on triangular
598 grids, part i: formulation and performance of the baseline version. *Geosci. Model Dev.*, **6**, 735–
599 763.

- 600 Williamson, D. L., 2002: Time-split versus process-split coupling of parameterizations and dy-
601 namical core. *Mon. Wea. Rev.*, **130**, 2024–2041.
- 602 Williamson, D. L., J. G. Olson, C. Hannay, T. Toniazzo, M. Taylor, and V. Yudin, 2015: Energy
603 considerations in the community atmosphere model (cam). *J. Adv. Model. Earth Syst.*, **7** (3),
604 1178–1188, doi:10.1002/2015MS000448, URL <http://dx.doi.org/10.1002/2015MS000448>.
- 605 Zarzycki, C. M., C. Jablonowski, and M. A. Taylor, 2014a: Using variable-resolution meshes to
606 model tropical cyclones in the community atmosphere model. *Mon. Wea. Rev.*, **142** (3), 1221–
607 1239, doi:10.1175/MWR-D-13-00179.1.
- 608 Zarzycki, C. M., M. N. Levy, C. Jablonowski, J. R. Overfelt, M. A. Taylor, and P. A. Ullrich,
609 2014b: Aquaplanet experiments using cam’s variable-resolution dynamical core. *J. Climate*,
610 **27** (14), 5481–5503, doi:10.1175/JCLI-D-14-00004.1.
- 611 Zhang, K., and Coauthors, 2017: Impact of numerical choices on water conservation in the e3sm
612 atmosphere model version 1 (eam v1). *Geoscientific Model Development Discussions*, **2017**,
613 1–26, doi:10.5194/gmd-2017-293.

614 LIST OF FIGURES

- 657 **Fig. 10.** Mean ω at two model levels in the middle troposphere, in a Held-Suarez configuration
 658 outfitted with real world topography. (Left) CAM-SE state on the GLL grid, *ne30np4*,
 659 (Middle) CAM-SE-CSLAM state on the GLL grid, *ne30np4* and (Right) CAM-SE-CSLAM
 660 state on the physics grid, *ne30pg3*. The ω fields are computed from a 1200 day Held-Suarez
 661 simulation. The data are contoured according to a ‘cell fill’ approach, in which the coupler
 662 grids (e.g., Figure 4) are used to delineate the vertices of the control volumes. 41

663 **Fig. 11.** Climatological total precipitation rate (in mm/day) computed from the final 19 years of a pair
 664 of 20 year long AMIP type simulations. (Left) CAM-SE, (middle) CAM-SE-CSLAM and
 665 (Right) their differences. The difference field is computed through bilinearly interpolating
 666 to a common latitude-longitude grid. 42

667 **Fig. 12.** Climatological total precipitation rate computed from the final 19 years of a suite of 20
 668 year long AMIP simulations, using CAM-SE (*ne30np4*), CAM-SE-CSLAM (*ne30np3*) and
 669 CAM-FV (*f09*). The top plot is an observational product, the gridded GPCP climatological
 670 precipitation dataset. 43

671 **Fig. 13.** Schematic of the coordinate system in which the dimensionally split cubic Lagrange
 672 interpolation is computed. The physics grid centers are marked with asterisks and the GLL
 673 points, we are interpolating to, with solid filled circles. The element in which the GLL
 674 points are located is bounded by thick black lines and located in the lower left corner of a
 675 panel. The stippled lines mark the boundaries of the remaining elements. For simplicity we
 676 are using the normalized coordinate centered at the element on which the GLL points we
 677 are interpolating to are located. Note that the coordinates for points on neighboring panels
 678 (using a different local coordinate system) must be transformed to the coordinate system of
 679 the element in question. 44

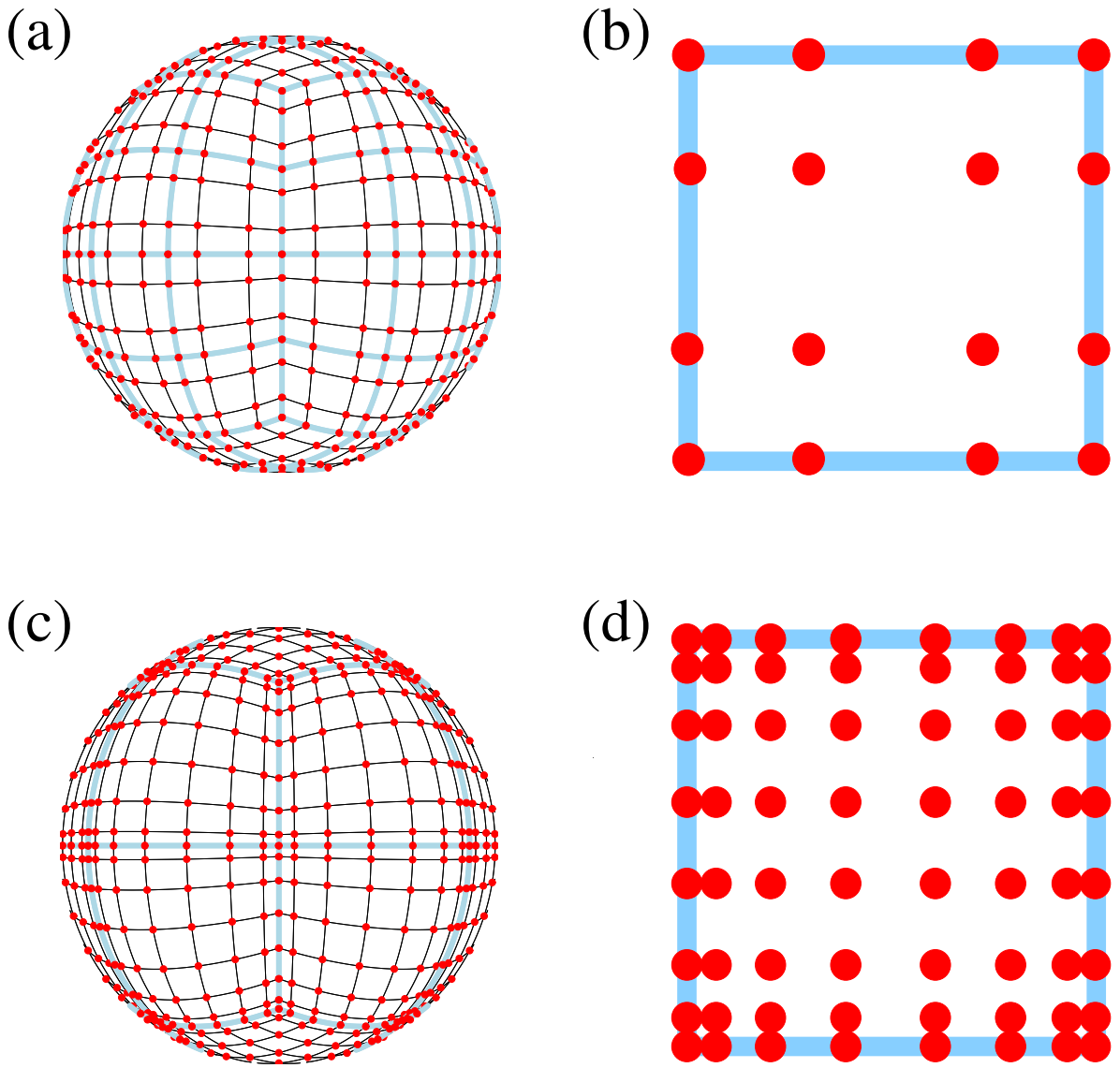
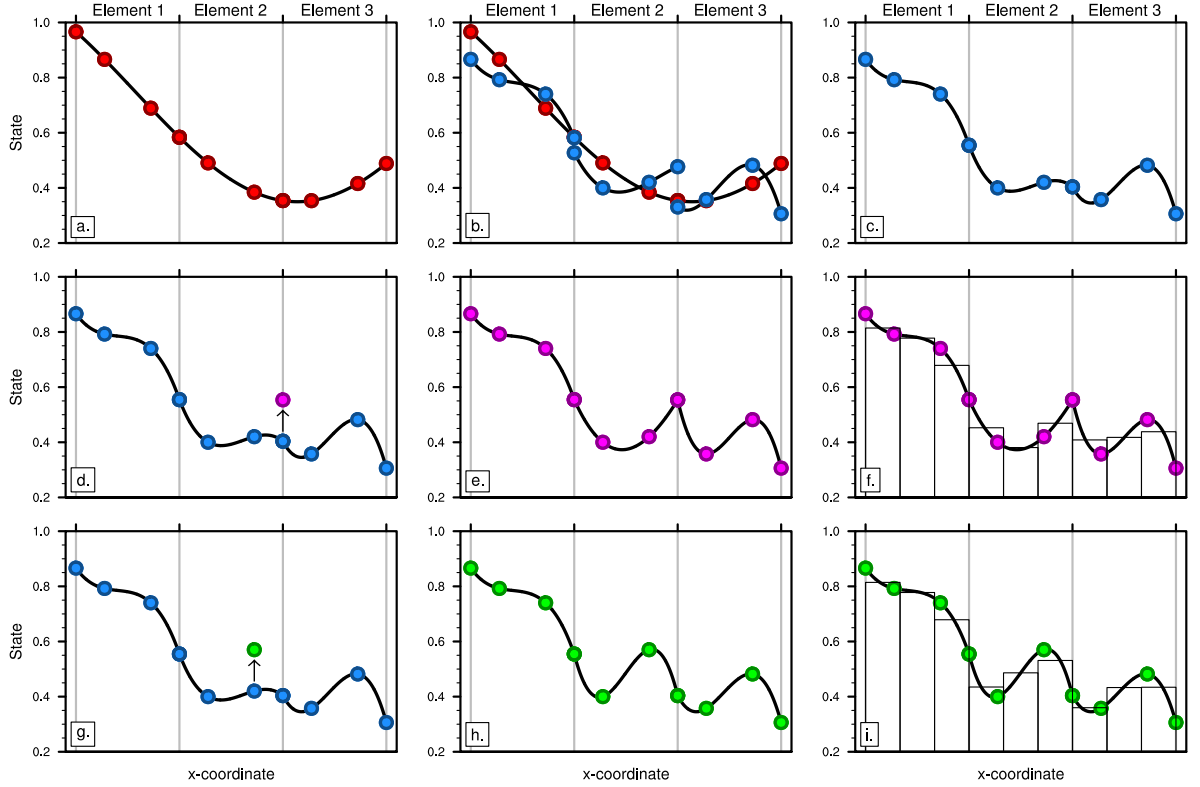
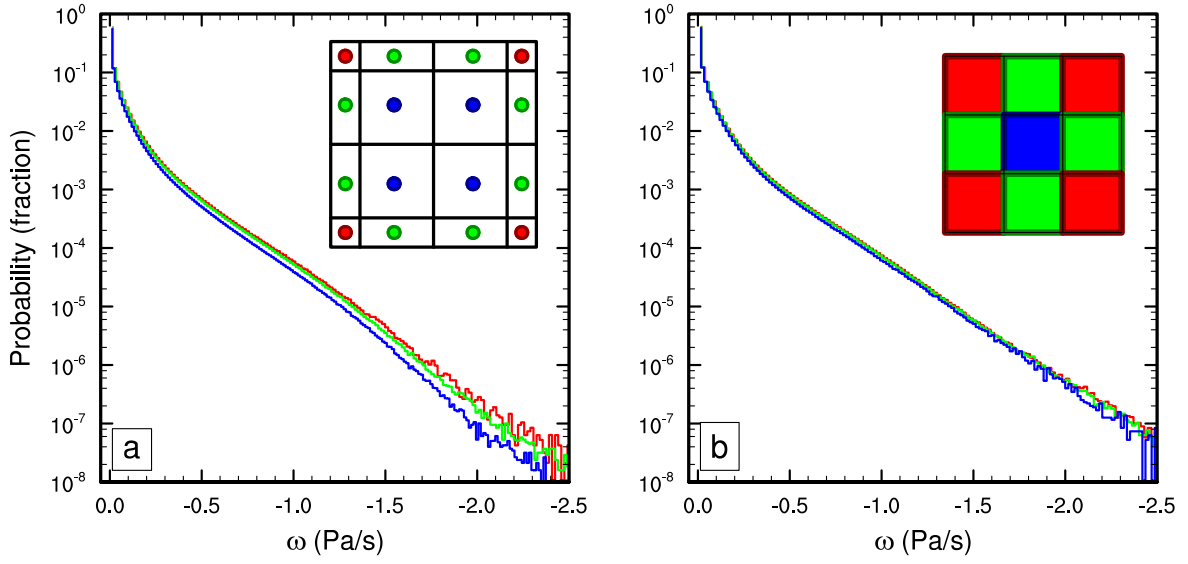


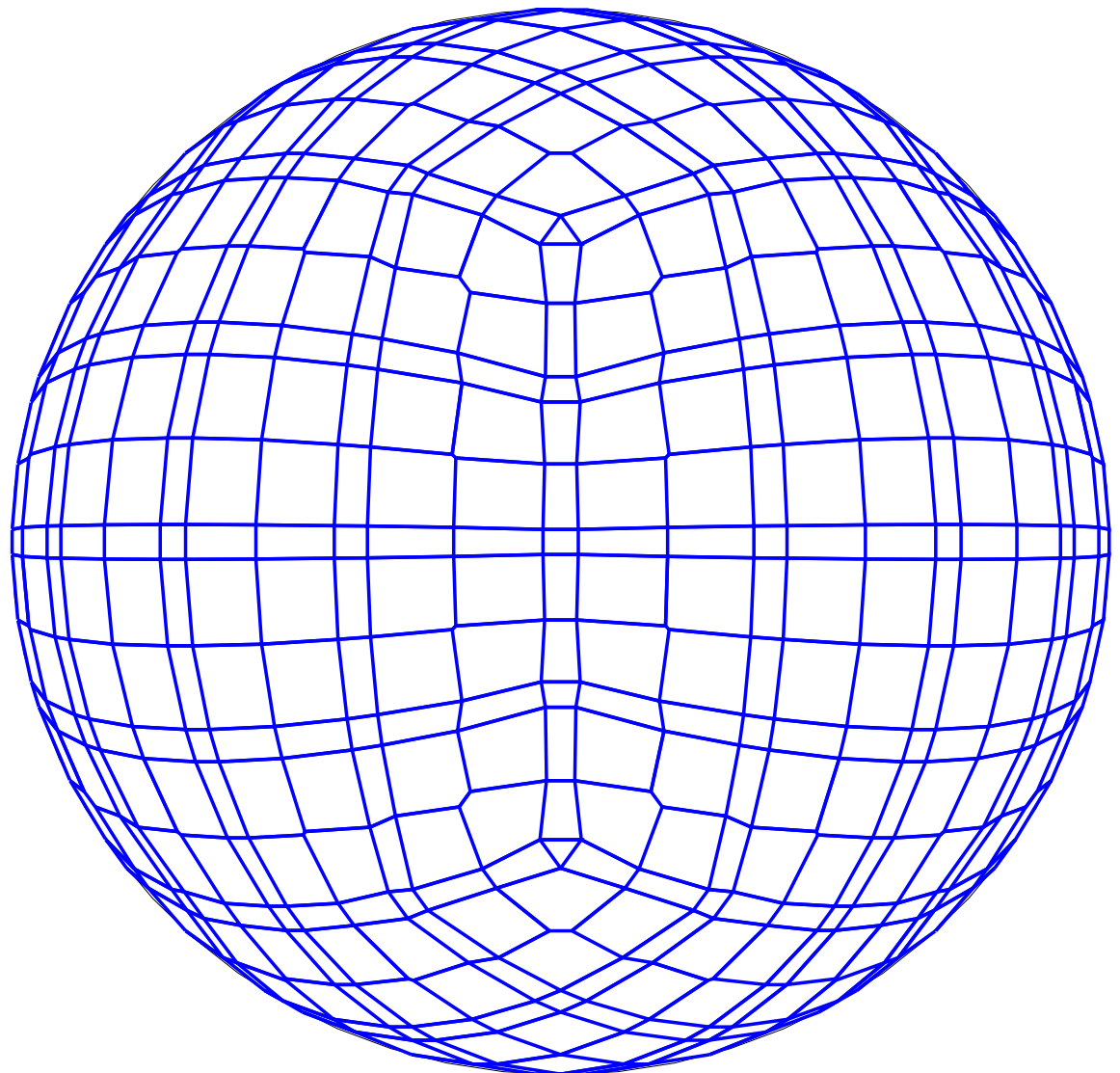
FIG. 1. Example of CAM-SE GLL quadrature grids, marked with red filled circles, (a & c) on the cubed-sphere and (b & d) in an element. (a)-(b) and (c)-(d) use 4×4 ($np = 4$) and 8×8 ($np = 8$) GLL quadrature points in each element, respectively. (a) and (c) have the same average grid-spacing at the Equator (7.5°) which is obtained by using (a) 4×4 ($ne = 4$) and (b) 2×2 ($ne = 2$) elements on each cubed-sphere face/panel, respectively. The element boundaries are marked with thick light blue lines. The grid configurations shown on (a) and (c) are referred to as $ne4np4$ and $ne2np8$, respectively.



686 FIG. 2. A one-dimensional schematic showing the relationship between the basis functions, the quadrature
 687 nodes and the proposed physics grid, over the coarse of a time-step. The filled circles are the GLL quadrature
 688 points in each element, which are connected by a Lagrange polynomials basis (curves). (a) Smooth initial con-
 689 dition are (b) advanced by the dynamics one Runge-Kutta step (blue), and (c) shows the solution after applying
 690 the DSS operator. Applying (d) grid-scale forcing to an element boundary node, (e) the basis representation is
 691 clearly C^0 at the element boundary. In contrast, (d) applying grid-scale forcing to an interior node (e) results
 692 in a smooth, C^∞ continuous field. (f),(i) Vertical bars pertain to the values on the physics grid, found through
 693 integrating the basis functions over the control volumes.

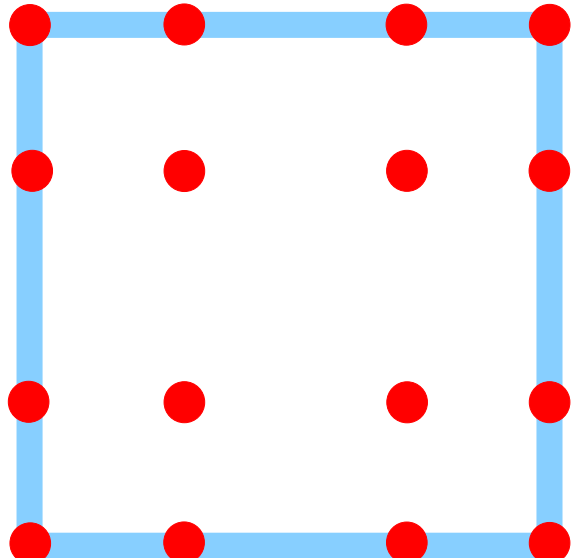


694 FIG. 3. Probability density distribution of instantaneous upward ω in a pair of aqua-planet simulations using
695 CAM4 physics. Figure is constructed from one year of six hourly data, at all vertical levels. (a) *ne30np4*
696 configuration conditionally sampled for interior, edge and corner node control volumes, and similarly (b) for the
697 *ne30pg3* configuration. Note the consistently larger magnitude ω for boundary nodes compared with interior
698 nodes in (a), and that the bias is substantially reduced through mapping to a quasi-equal area physics grid.

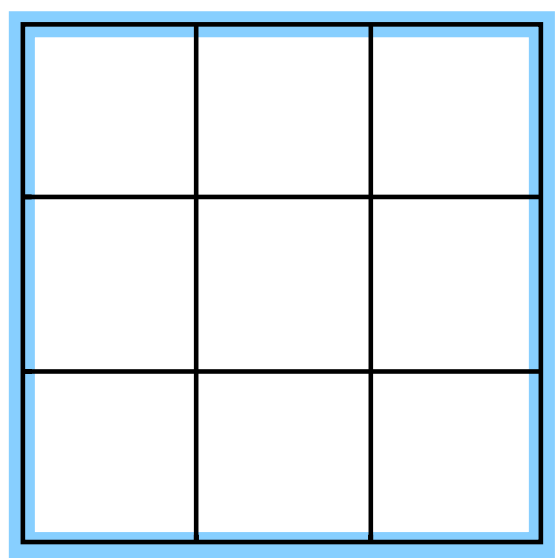


699 FIG. 4. An example of control volumes constructed around GLL quadrature points ($ne4np4$) so that the
700 spherical area of the control volumes exactly match the quadrature weight multiplied by the metric factor.

$$np = 4$$



$$pg = 3$$



701 FIG. 5. A schematic illustration of an element, indicating the relationship between (left) the dynamical core
702 grid, and (right) the proposed quasi-equal area physics grid. The physics grid contains $pg \times pg = 3 \times 3$ grid cells
703 in each element.

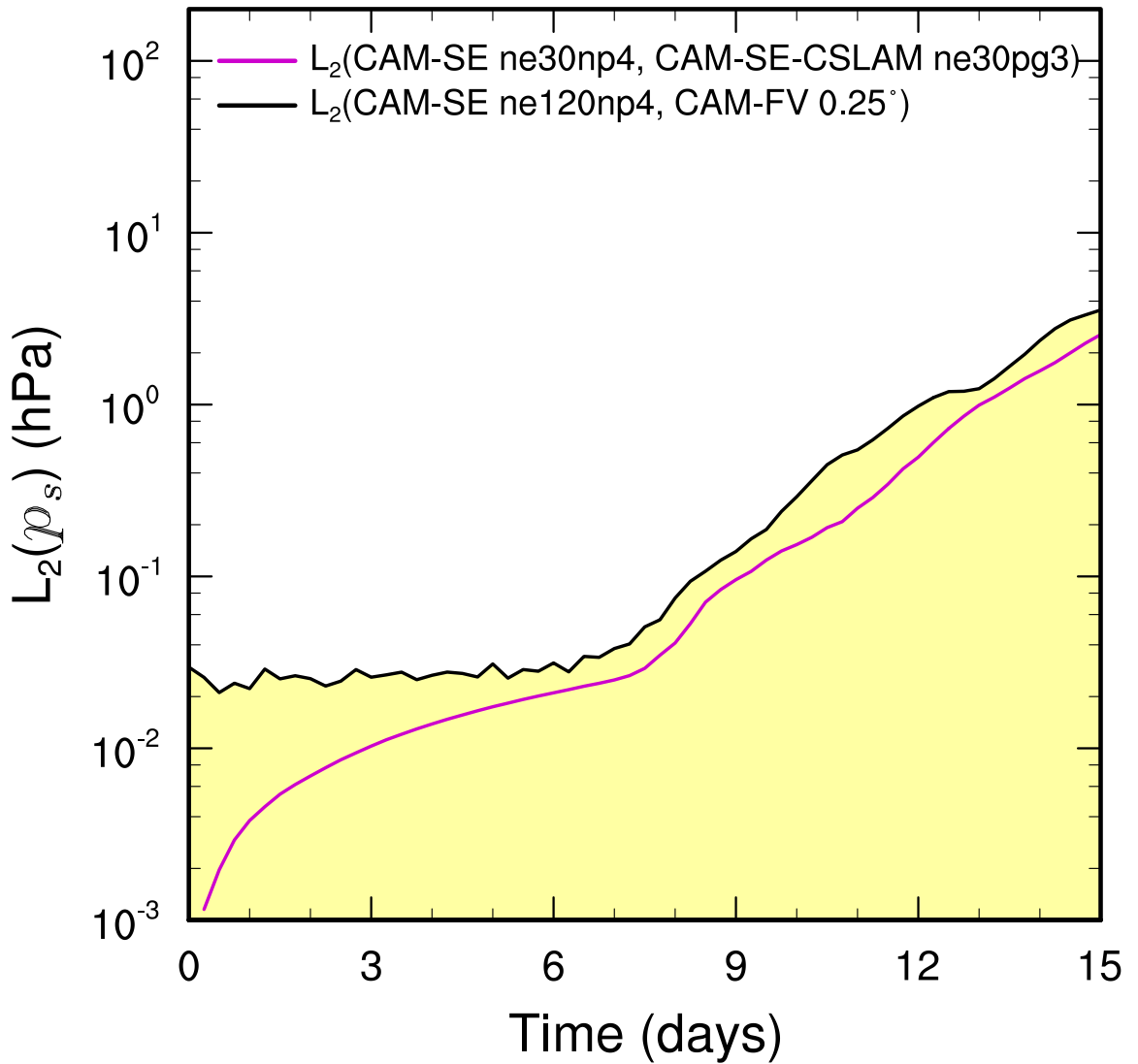


FIG. 6. L_2 difference norms of the surface pressure field, p_s , in the moist baroclinic wave simulations. L_2 values lying within the yellow region fall below the estimate of the uncertainty in the reference solution (black curve), computed as the difference norm between two approximately 0.25° resolution versions of CAM, the spectral-element and finite-volume (CAM-FV) dynamical cores.

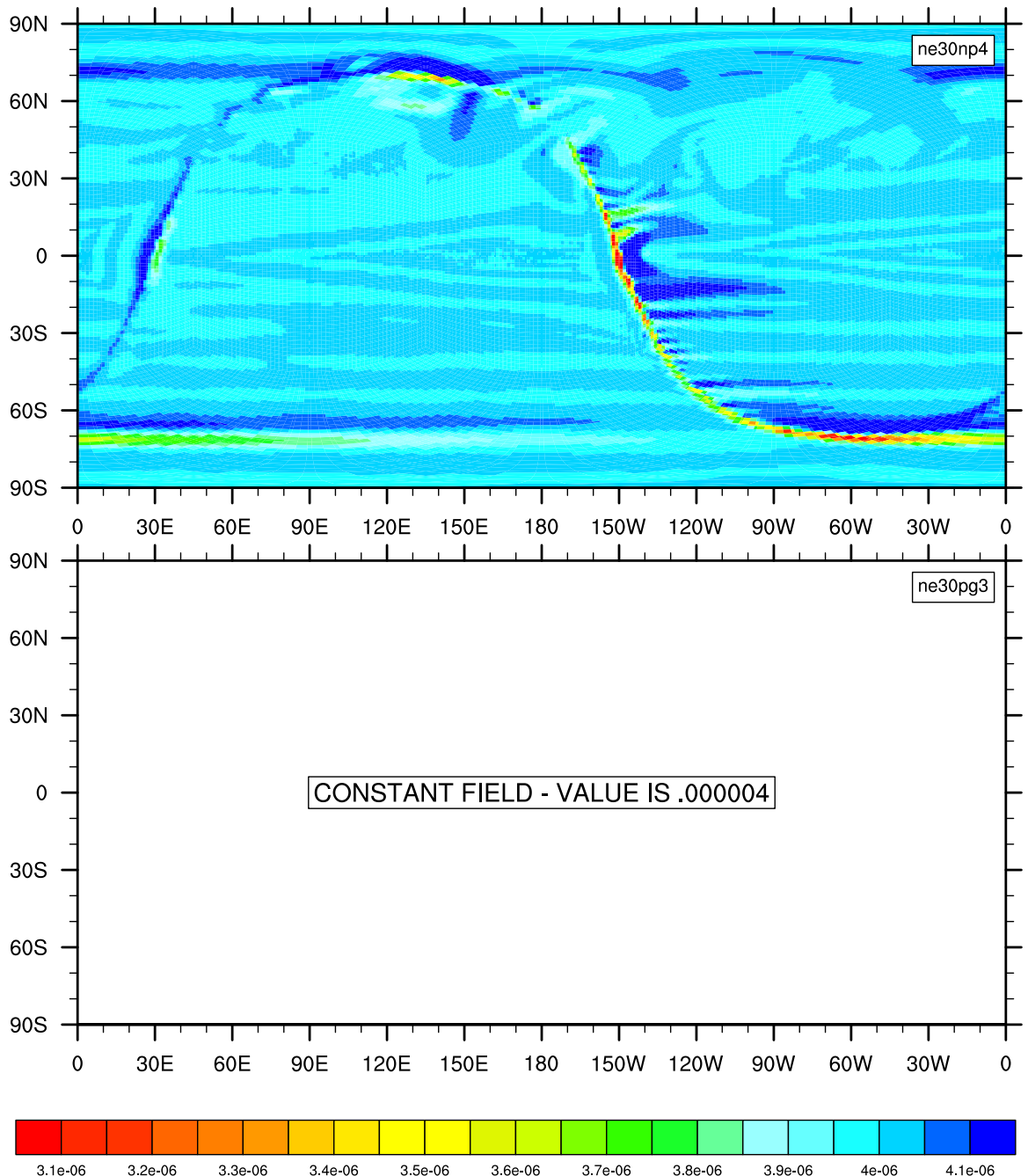
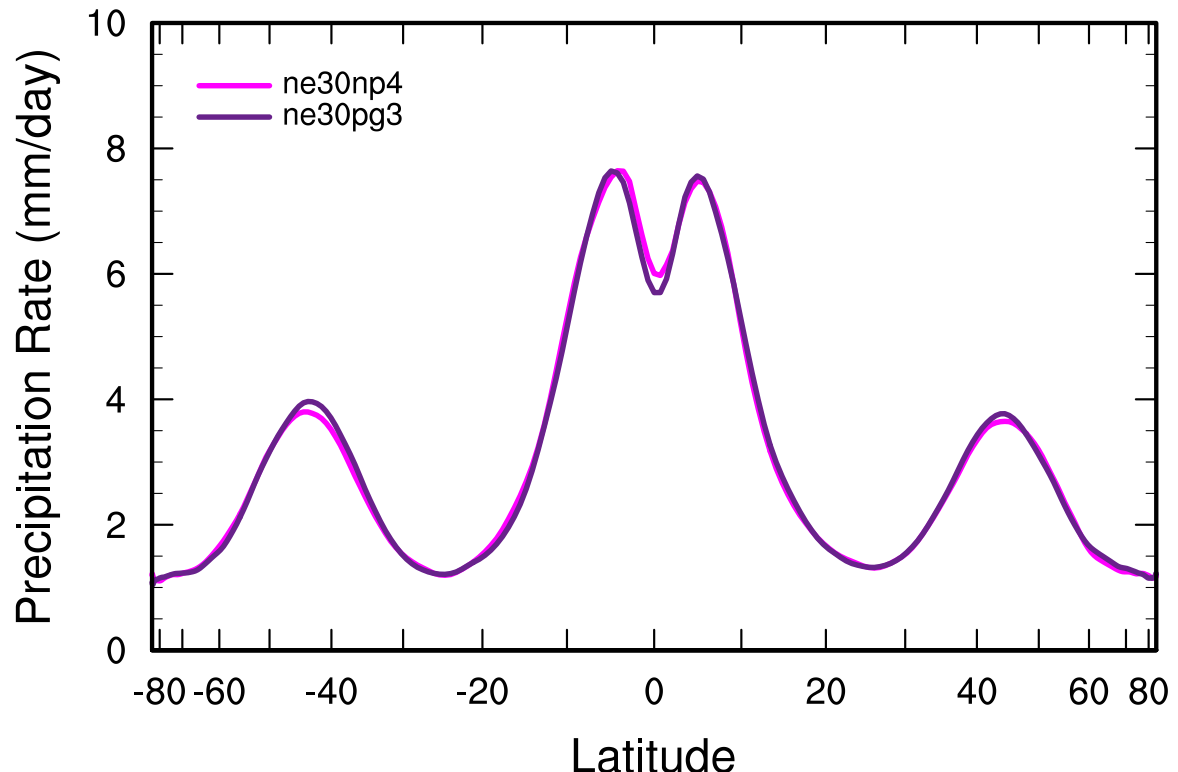
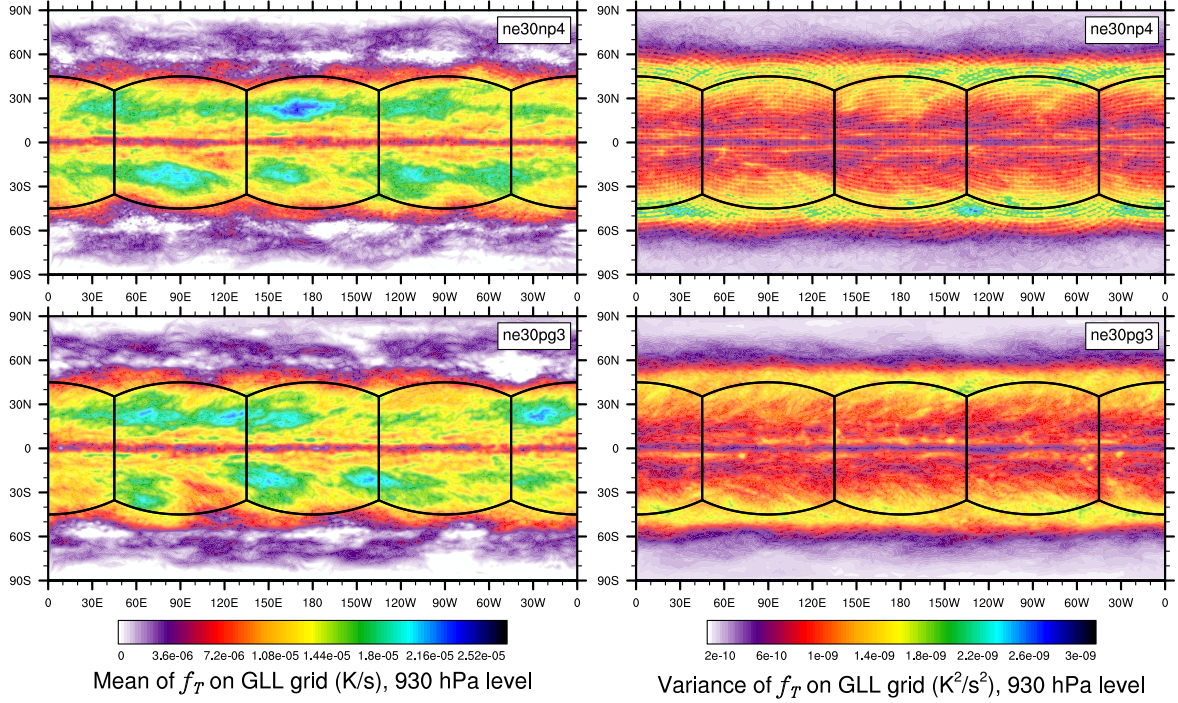


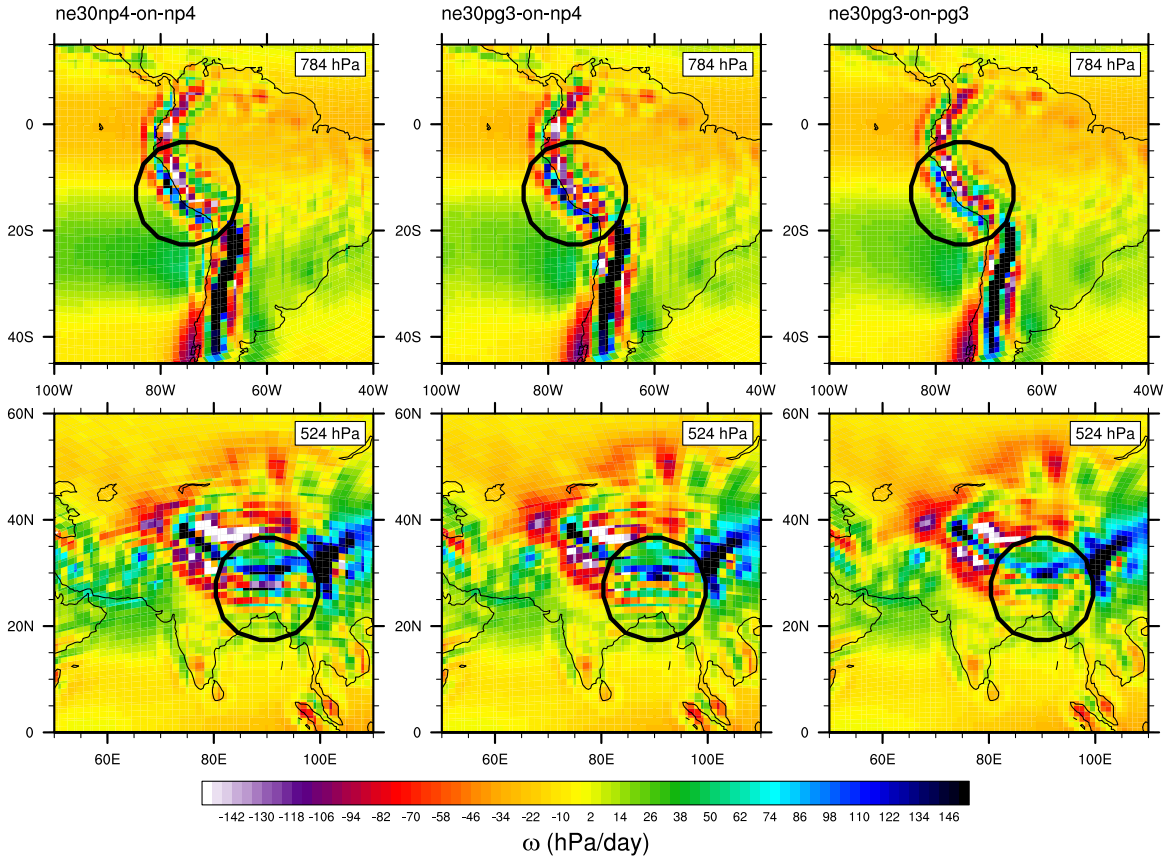
FIG. 7. Results of the terminator "toy"-chemistry test. Snapshot of the total column tracer mass at day 15 of
 708 the moist baroclinic wave test. (Top) CAM-SE, (Bottom) CAM-SE-CSLAM.
 709



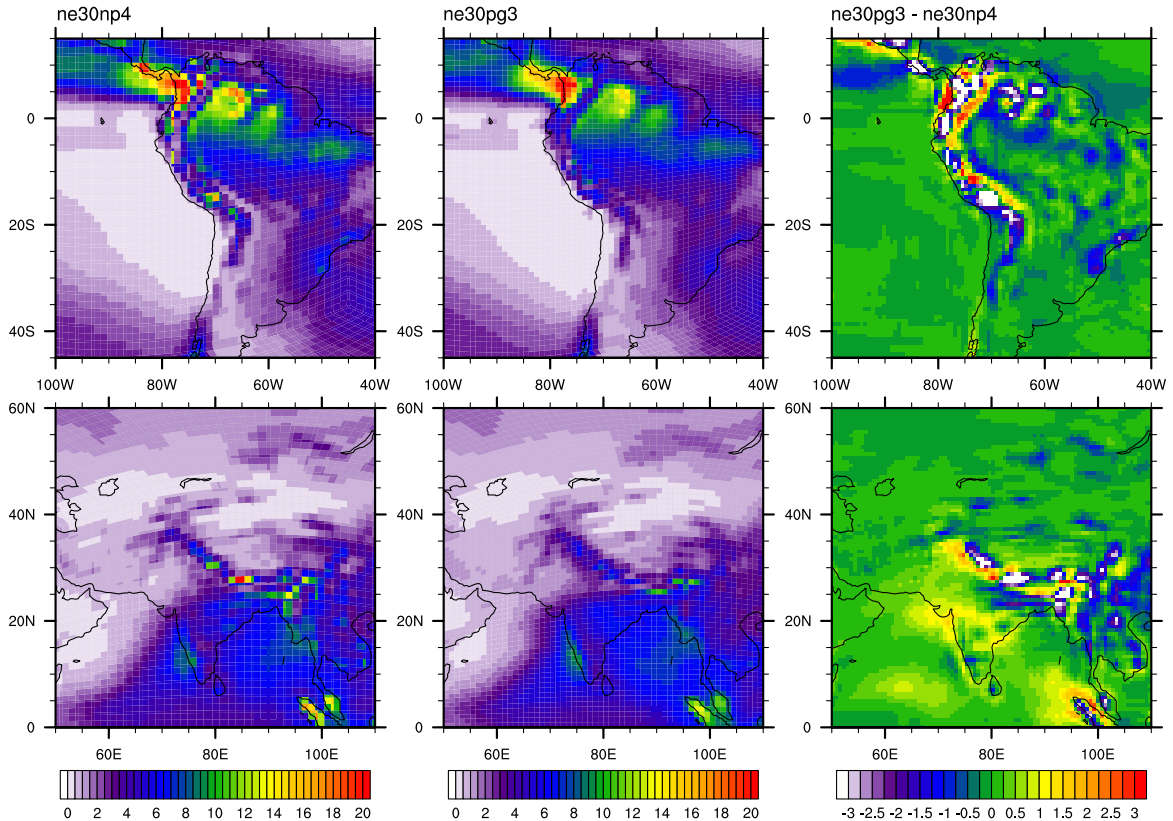
710 FIG. 8. Climatological zonal-mean total precipitation rate in the aqua-planets, computed from a pair of year
711 long simulations.



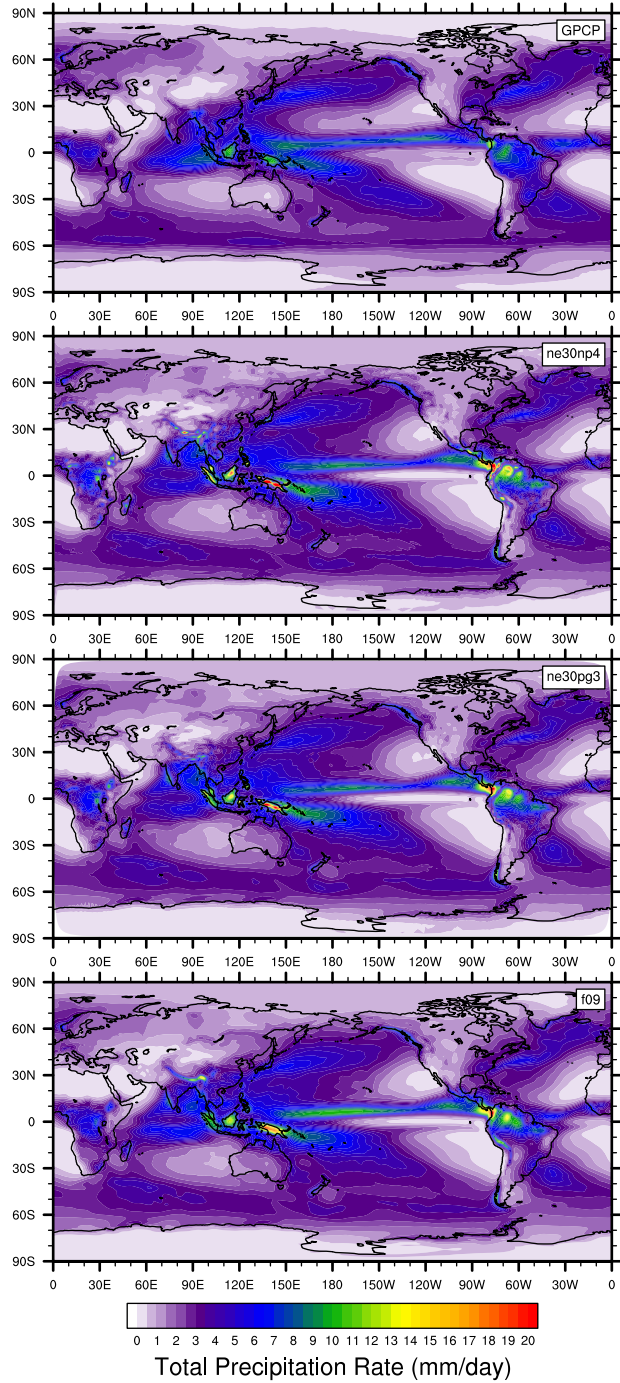
712 FIG. 9. Mean (left) and variance (right) of the low level temperature tendencies from the physical parameteri-
 713 zations on the GLL grid, with the ne30np4 configuration, (top row) and ne30pg3 configuration (bottom row), in
 714 a pair of year-long aqua-planet simulations after Medeiros et al. (2016). Grid imprinting is observed along the
 715 element boundaries in ne30np4, but is absent from the ne30pg3 simulation.



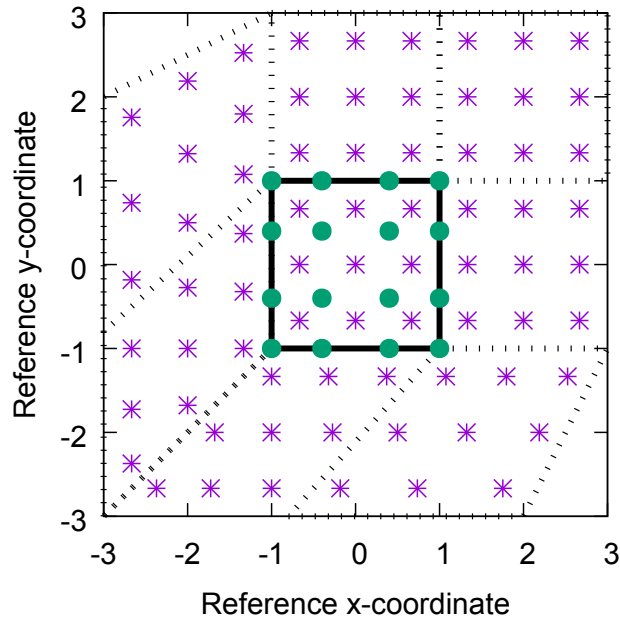
716 FIG. 10. Mean ω at two model levels in the middle troposphere, in a Held-Suarez configuration outfitted with
 717 real world topography. (Left) CAM-SE state on the GLL grid, *ne30np4*, (Middle) CAM-SE-CSLAM state on
 718 the GLL grid, *ne30np4* and (Right) CAM-SE-CSLAM state on the physics grid, *ne30pg3*. The ω fields are
 719 computed from a 1200 day Held-Suarez simulation. The data are contoured according to a ‘cell fill’ approach,
 720 in which the coupler grids (e.g., Figure 4) are used to delineate the vertices of the control volumes.



721 FIG. 11. Climatological total precipitation rate (in mm/day) computed from the final 19 years of a pair of 20
 722 year long AMIP type simulations. (Left) CAM-SE, (middle) CAM-SE-CSLAM and (Right) their differences.
 723 The difference field is computed through bilinearly interpolating to a common latitude-longitude grid.



724 FIG. 12. Climatological total precipitation rate computed from the final 19 years of a suite of 20 year long
 725 AMIP simulations, using CAM-SE (ne30np4), CAM-SE-CSLAM (ne30np3) and CAM-FV (f09). The top plot
 726 is an observational product, the gridded GPCP climatological precipitation dataset.



727 FIG. 13. Schematic of the coordinate system in which the dimensionally split cubic Lagrange interpolation
 728 is computed. The physics grid centers are marked with asterisks and the GLL points, we are interpolating to,
 729 with solid filled circles. The element in which the GLL points are located is bounded by thick black lines and
 730 located in the lower left corner of a panel. The stippled lines mark the boundaries of the remaining elements.
 731 For simplicity we are using the normalized coordinate centered at the element on which the GLL points we are
 732 interpolating to are located. Note that the coordinates for points on neighboring panels (using a different local
 733 coordinate system) must be transformed to the coordinate system of the element in question.